Microstructure formation in 6061 aluminum alloy during nano-second pulsed laser processing

D. Zhemchuzhnikova, Julien Zollinger

Microstructure formation in 6061 aluminum alloy during nano-second pulsed laser processing

D. Zhemchuzhnikova*, J. Zollinger

Université de Lorraine, Institut Jean Lamour, Campus ARTEM, Allée André Guinier, 54011, Nancy, France.

Abstract. Pulsed lasers are very promising branch of the laser material processing in terms of high productivity and quality of the resulting welds. However, laser welding of Al-based alloys is challenging due to their solidification hot cracking susceptibility. In this paper, AA6061 alloy, one of the widely used engineering materials, was processed with a nano-second pulsed welding in the keyhole mode. The influence of process parameters, such as the laser power and the pulse duration, on the weld seam microstructure and geometrical characteristics was investigated. It was found that this welding allows to produce crack-free welds for all tested processing conditions. Unexpectedly, the lack of visible dendritic structure as well as heat affected zone (HAZ) in the weld pool were observed. These phenomena were explained by extremely high temperature gradients determined from the geometrical analysis of the weld pools, and were confirmed by solidification microstructure modeling.

Keywords: laser processing, microstructure formation, aluminum alloy, keyhole mode, temperature gradient, solidification modeling

*Corresponding author. E-mail addresses: daria.zhemchuzhnikova@gmail.com

Published in Journal of Materials Processing Technology 314, 117898
doi:https://doi.org/10.1016/j.jmatprotec.2023.117898

1. Introduction

After the invention of laser-based technology by Maiman at Hudges Aircraft Company in 1960 (Mainman, 1960), more and more laser industrial applications have been identified. According to Schmidt et al. (2018), the widespread use of laser technology for marking, engraving, cutting, and micromachining have led to a doubling of the world market for laser processing of materials over the last decade. Recently, specific functional needs together with high growth rates in markets such as aviation, automotive industries and micro-electronics, attracted special attention to use of laser sources for welding and joining processes (Gabzdyl and Rosowski, 2017). Such extensive application of laser welding is associated with advantages it offers over the conventional welding techniques: precise heat input resulting to minimal distortion in the jointed zone, wide range of welded materials including dissimilar pairs, as well as joining of thin materials and the possibility to weld without filler wire. In addition, this is a flexible high-quality high-speed technology that can be easily integrated into a production line.

Aluminum alloys are one of the most widely used metal structural materials, however, its laser welding is challenging due to their high reflectivity, low viscosity and high thermal conductivity. Nevertheless, these problems can be successfully solved by optimizing the welding process parameters. For example, high reflectivity and thermal conductivity of Al-based alloys can be compensated by the choice of laser source. Cieslak and Fuerschbach (1988) discussed that among the higher power laser welding system Nd:YAG laser offers better absorptivity than the CO_2 laser. Later on, Bergmann et al. (2013) have shown an improvement of the welding quality of aluminum with a decrease of defects number by superposition of a pulsed Nd:YAG laser with a diode laser. The laser beam absorption can also be increased when a keyhole is formed due to multiple reflections of the beam in the

keyhole (El-Batahgy and Kutsuna, 2009). Pulsed wave mode of the laser source provides more accurate temperature control which results in minimal thermal impact and reduces the HAZ (Assuncao and Williams, 2013).

Many wrought aluminum alloys, especially the 6xxx series, are known to be susceptible to solidification hot cracking (Çam and İpekoğlu, 2017). The grain structure of the weld is the major influence on the susceptibility to hot cracking. Hagenlocher et al. (2019) demonstrated that the tendency to hot cracking can be reduced by the presence of high number of grain boundaries across the width of the weld seam. It was shown that this effect could be achieved by a grain size reduction or an enlargement of the width of the equiaxed grain structure zone. Tang and Vollertsen (2014) developed an analytical model to investigate the influence of grain size and equiaxed grains fraction on the AA6082 laser welds hot cracking susceptibility. The model determined that minimal hot cracking susceptibility will be reached with the grain size of 25 μm and the fraction of equiaxed grains of 100 % which was confirmed by the experimental data. In addition, as shown by Wang et al. (2016), the weld microstructure refinement plays a particularly important role for heat-treatable aluminum alloys since it can minimize the softening effect of the fusion zone due to the strengthening precipitates dissolution.

In general, there are two possibilities to optimize the grains morphology of the fusion zone. The first one is alloying additives that promote nucleation and refined grain structure. This was used, for example, by Tang and Vollertsen (2014) when different amounts of titanium and boron were added in the weld metal of AA6082. The other approach is based on the variation of process parameters to influence the solidification conditions. Wang et al. (2016) shown that beam oscillation during laser welding of AA6061-T6 promoted the formation of equiaxed grains within the fusion zone due to stirring effect. Chua et al. (2019)

demonstrated that the most important factor to affect weld geometry is laser peak power applied in the welding process.

The current study investigates the influence of process parameters of ultra-fast nano-second pulsed laser welding on the microstructure formation of commercial 6061 aluminum alloy. This alloy is generally not prone to welding without filler metal. It is shown that by achieving extremely high temperature gradients, nano-second pulsed laser welding allows to produce crack-free welds by growing dendrite-free microstructures.

2. Materials and methods

The material used in this research was commercially available 6061 aluminum alloy in T4 state (composition in wt.%: 1.53 Mg, 0.45 Si, 0.43 Cu, 0.5 Fe, 0.17 Cr, 0.1 Mn). The size of the sample was 2.5 mm thick, 50 mm wide and 50 mm long. The grain structure of the initial material primarily consisted of the coarse grains of ~ 40 μm long and ~ 15 μm thick. Coarse Fe-rich second phase particles up to tens of microns in size were uniformly distributed in aluminum matrix (Fig. 1). From Energy Dispersive X-Ray Spectroscopy (EDS), the Fe:Si atomic ratio of these intermetallic particles was close to 2, which corresponds to α-Al(Fe,Mn)Si phase (Hosseinifar and Malakhov, 2011).

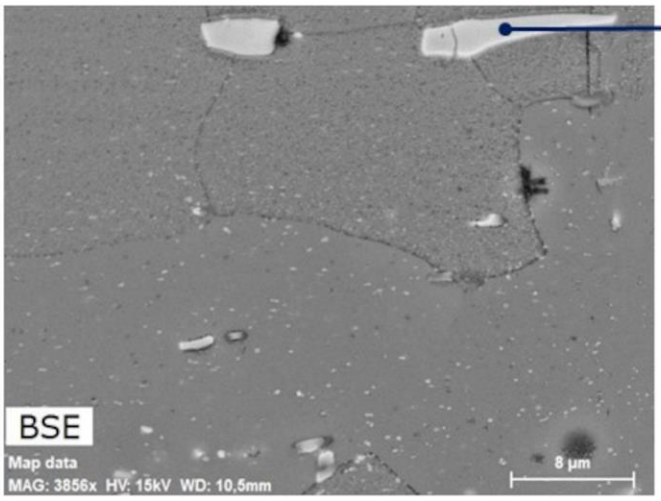

Element	atom. %
Al	72.90
Fe	16.62
Si	8.44
Mn	1.25
Cr	0.79

Fig. 1. SEM micrograph of the base material.

The laser source employed for experiments was a pulsed ytterbium fibre laser with beam quality parameter $M^2 < 1.3$. The laser beam was focused on the top surface of the substrate in a spot of 30 μm diameter. Keyhole mode welding was performed without shielding gas with a welding speed of 40 mm/s and a pulse frequency (PF) of 100 kHz. Other parameters, mainly average power (P_a) and pulse duration (PD), were varied and their combinations for each fusion line are presented in Table 1. It should be noted that the pulse energy (E_p) and average peak power (P_{AP}) in Table 1 are calculated parameters. Similar to Abioye et al. (2019), they were determined as $E_p = P_a/PF$ and $P_{AP} = E_p/PD$.

Table 1
Laser welding experimental parameters.

Line number	Average power [P_a], W	Pulse duration [PD], ns	Pulse energy [E_p], mJ	Average peak power [P_{AP}], kW
1	30		0.3	1.5
2	21	200	0.21	1.05
3	12		0.12	0.6
4	30		0.3	3
5	21	100	0.21	2.1
6	12		0.12	1.2
7	30		0.3	6
8	21	50	0.21	4.2
9	12		0.12	2.4

After laser welding samples for optical microscopy (OM) were prepared by mechanical polishing in conventional fashion, followed by the final etching in standard Keller's reagent (0,5 HF-1,8 HCl2-2,7 HNO3-95 H2O, in wt.%). A final surface finish for scanning electron microscopy (SEM) was obtained by a standard metallographic polishing up to 1 μm followed by an OPS finish. The foils for TEM examination were prepared using a focused ion beam (FIB)-SEM dual beam system (FEI Helios 600) using the 'in-situ' lift-out technique. Transmission electron microscopy (TEM) investigations were carried out using a JEM - ARM 200F Cold FEG TEM/STEM operating at 200 kV and equipped with a spherical

aberration (Cs) probe and image correctors (point resolution 0.19 nm in TEM mode and 0.078 nm in STEM mode). The elemental composition was evaluated by SEM-EDS in spot and area scan modes. To visualize the grain structure and characterize misorientations of grain and subgrain boundaries, electron back scattering diffraction (EBSD) analysis was performed. For that, samples surfaces were prepared by ionic polishing. In the present study high-angle boundaries (HABs) were defined for grain misorientations ≥15°; low-angle boundaries (LABs) corresponded to the misorientations within the range of 2-15°. In the EBSD map, LABs and HABs are depicted as white and black lines, respectively.

3. Results

3.1 Influence of process parameters on weld pool geometry

The cross-sections of weld lines obtained for different process parameters are presented in Fig. 2. As can be seen, the line profiles are slightly inclined. According to Fabbro and Chouf, (2000) this effect is due to multiple beam reflection which leads to unstable geometry of front keyhole wall during deep penetration laser welding. Table 2 summarizes the penetration depth and width of each weld determined from these images. In general, the higher average peak power leads to higher penetration depth (Fig. 2, Table 2). Similar effect was described by Ascari et al. (2017) where the peak pulse power was identified as the most influential process parameter responsible for the penetration depth and width of the weld. On the other hand, for lines obtained at similar peak power, for example, for line 2 at 1.05 kW and for line 6 at 1.2 kW, the change in pulse duration was also influencing the depth of penetration, with depth increasing with PD increasing. Its value is 225 μm at PD=200 ns and 180 μm at PD=100 ns for line 2 and line 6, respectively (Table 2).

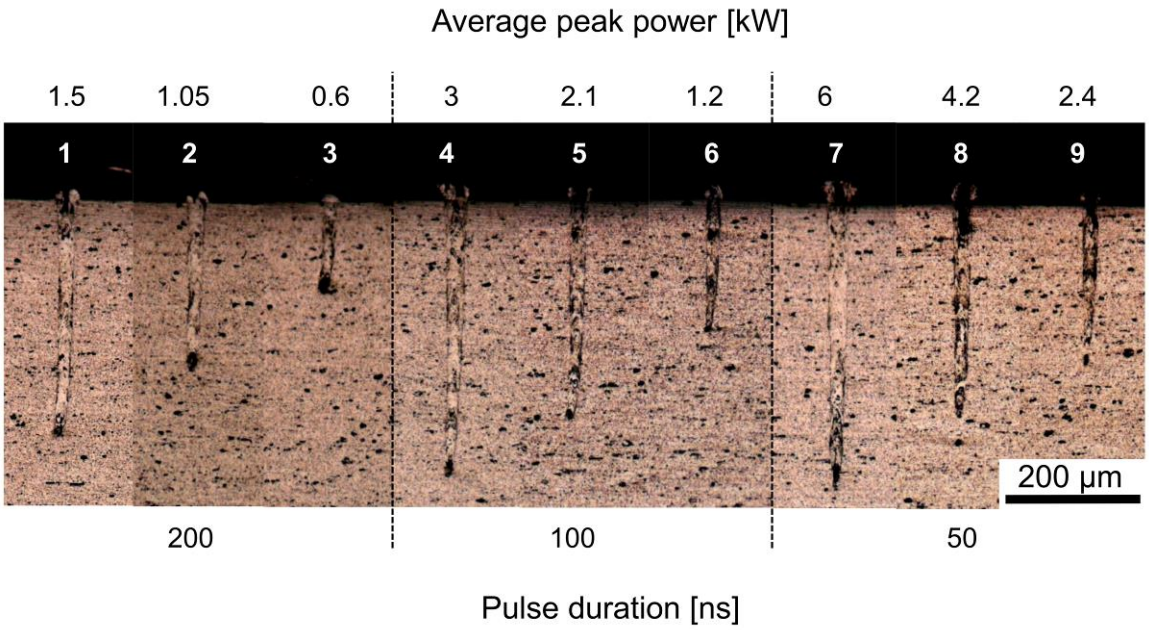

Fig. 2. OM photos of etched cross section of fusion lines obtained at various process parameters.

Table 2
Penetration depth and width of lines in Fig. 2.

Line number	P_{AP}, kW	Depth of penetration, µm	Weld width, µm
1	1.5	320	32
2	1.05	225	28
3	0.6	190	25
4	3	373	36
5	2.1	295	28
6	1.2	180	22
7	6	383	34
8	4.2	290	28
9	2.4	218	23

The quantitative relationship between penetration depth with both laser peak power and pulse duration is shown in Fig. 3(a). According to this Fig., with the same peak power, the longest pulse duration provides the highest penetration depth. Also, Fig. 3(a) clearly confirms the above-described observation: the penetration depth is increased with the growth of the peak power. Previous studies have reported that the higher peak power at the beginning of the pulse accelerates the absorption of laser photons by the metal surface, a first step in the

welding process also defined as coupling. The coupling is rapidly enhanced as the temperature increases (Kelkar, 2008). Meantime, longer pulse duration leads to higher surface temperature and longer energy absorption time, as reported theoretically by Kim and Ki (2014) and shown experimentally by Yusof et al. (2021). Therefore, both factors affect the weld penetration depth and its variation might be explained by their cumulative effect.

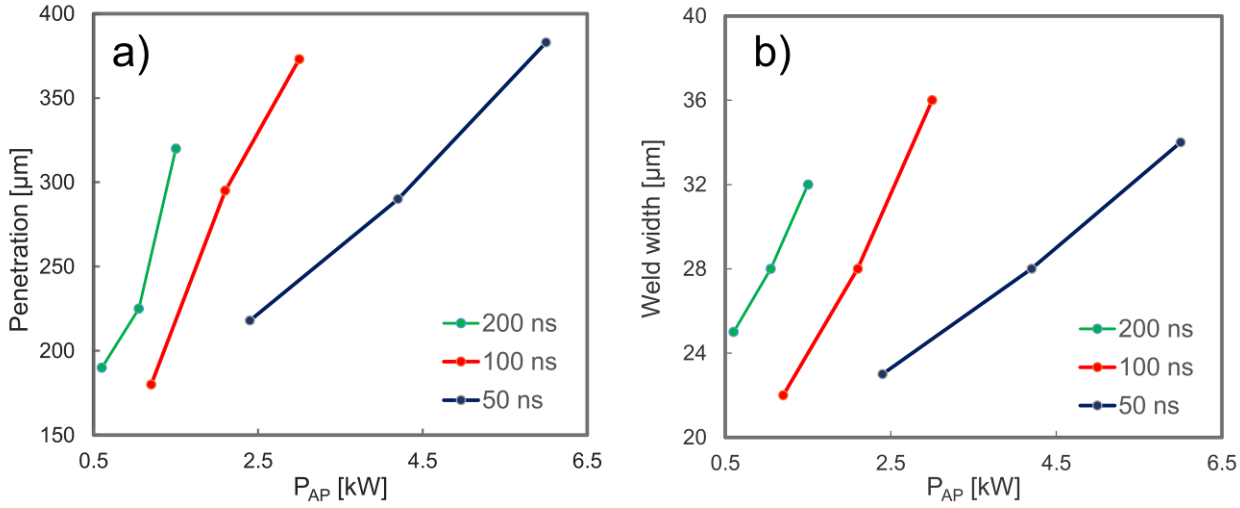

Fig. 3. Penetration depth (a) and weld width (b) variation from different power and pulse duration.

A similar trend was recorded for the weld width at the change in peak power and pulse duration (Fig. 3b). Accordingly, the previous conclusion about the simultaneous effect of these process parameters can be used in this case as well.

3.2 Solidification Microstructures

3.2.1 Defects

For all lines, the only defect observed is porosity, with holes and cavities of different sizes that can be observed even at low magnification in Fig. 2. A more detailed view is given in Fig. 4 that shows SEM images of the weld pools of lines 1 and 7. As can be seen in Figs. 2

and 4, the biggest cavities are located close to the top surface and at the keyhole roots. These pores have been initiated by convection movement of liquid aluminum going up from the bottom of the melt which is a common occurrence during laser welding in keyhole mode (Haboudou et al., 2003). Smaller round shape pores are observed mostly at the edges of the weld, as illustrated in the inserts in Fig. 4. Their number and surface fraction increased with increasing the laser average peak power. The weld pool from line 1 corresponds to a P_{AP} = 1.5 kW and line 6 to P_{AP} = 6 kW, and while not quantified here, the pores density is significantly reduced for low P_{AP} values. It has to be mentioned that despite the propensity of AA 6XXX alloys to solidification cracking during welding, particularly with laser processing without filler metal (Löveborn et al., 2017), no solidification cracking was observed. This will be discussed in details in section 4.

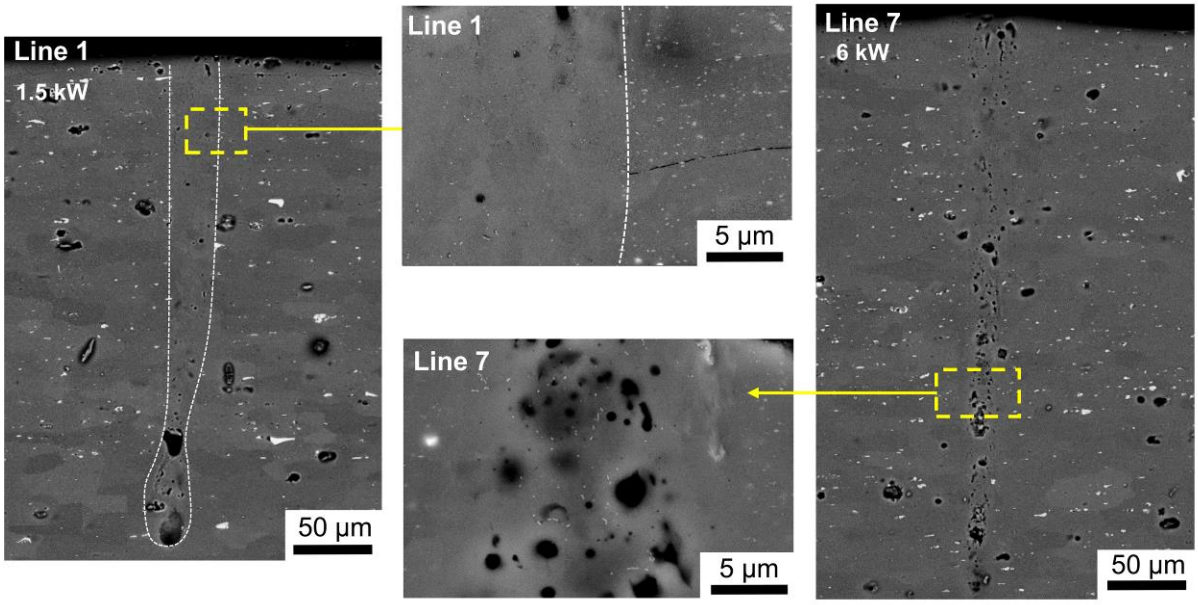

Fig. 4. SEM images of cross section of fusion lines obtained at different peak power. The fusion zone is highlighted by a dashed line.

3.2.2 Microstructure characterisation

A closer view of the weld microstructure is presented in Fig. 5(a) and (b) for the line 1. The coarse α-Al(Fe,Mn)Si particles observed in the base material are dissolved during welding and are no longer observed in the weld pool. As a result, the amounts of Fe and Si measured by EDS in the Al matrix (in precipitate-free areas) in the welding zone is higher than in the base material, in particular the amount of Fe goes from 0.1 in the base material to 0.47 in the weld pool. This is an indication that the solidification is out-of-equilibrium and allows to supersaturate the Al solid solution without further phase formation during the solidification. TEM-EDS maps of the fusion zone demonstrate very fine Fe-Si-rich precipitates or clusters which, in view of their size, (~ 10 nm) (Fig. 5b) are probably formed during natural aging.

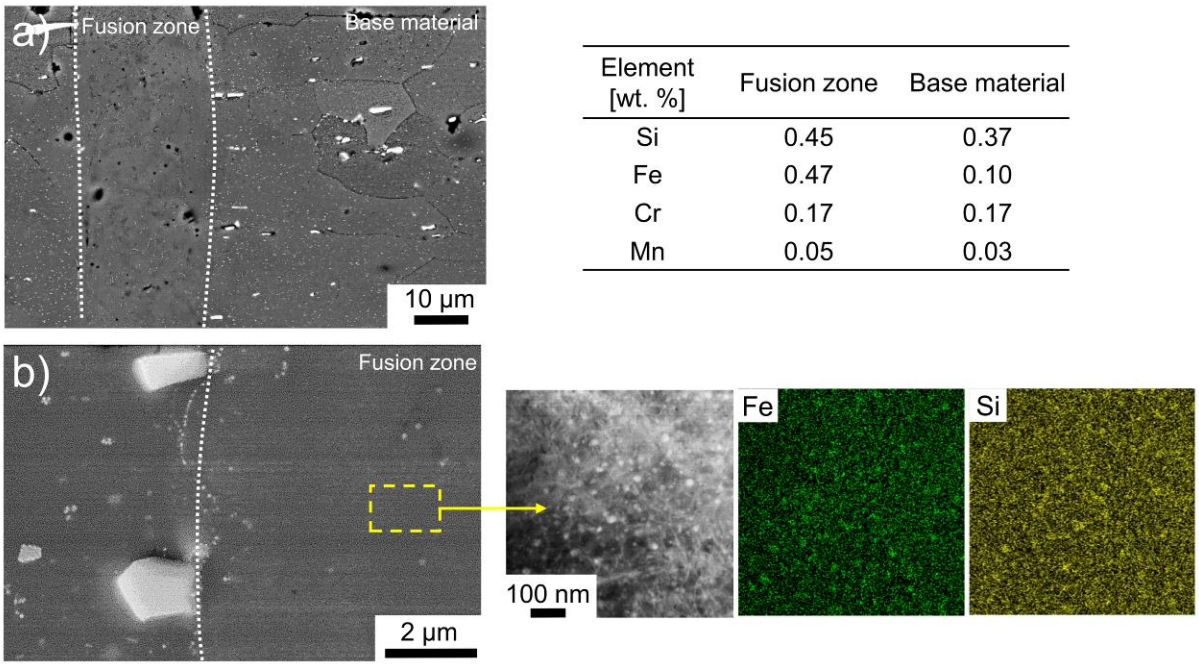

Element [wt. %]	Fusion zone	Base material
Si	0.45	0.37
Fe	0.47	0.10
Cr	0.17	0.17
Mn	0.05	0.03

Fig. 5. SEM images of: (a) line 1 and chemical composition of indicated zones; (b) example of the interface between the base material and the fusion zone, and element distribution in the fusion zone. The interface is highlighted by dotted lines.

Another surprising observation from the SEM-BSE images is the lack of visible dendritic structure in the weld pool which is usually observed in the welds of the 6XXX aluminum alloys (Fahimpour et al., 2012). Moreover, the HAZ resulting from the welding process is absent or very narrow; it could not be detected with the characterization techniques used in

the present study. Two α-Al(Fe,Mn)Si particles of the base material located at the interface between base material and weld pool are shown in Fig. 5(b). Such particles are usually elongated in the rolling direction and have a typical width to length ratio of 5:1 (Fig. 1). From Fig. 5(b) it seems that the particles have been "thermally" cut during the welding stage. The surviving parts of the α-Al(Fe,Mn)Si particles look unaffected confirming the narrow character of a possible HAZ, and seem to involve very high thermal gradient.

In order to provide additional insights to the samples' microstructure, EBSD analysis was performed for fusion lines with lower porosity, namely lines 1-3. The obtained EBSD maps with IPF colouring parallel to the welding direction are presented in Fig. 6. As can be seen, the microstructure in the weld pool can be divided in two categories. First, the grains grow by epitaxy from the base material, as an orientation continuity can be observed between base material and weld. In the three welding lines, the centerline consists in a region of small equiaxed grains. Distribution of these small grains along the depth of the weld pool is not uniform. Generally, the fine-grained regions were detected close to the top and in the middle of the weld (Fig. 6). The average grain size and surface fraction of the equiaxed grain size for the different P_{AP} values for lines 1-3 are reported in Table 3. Despite the difference in peak average power values during welding, the average size of these grains as well as their surface fraction are relatively constant for all conditions (within the uncertainty) and are ~ 1.3 μm and ~ 10 %, respectively. Also, no peculiar orientation relationships were found between the equiaxed grains which could have originated from ISRO mediated nucleation mechanism (Rappaz et al., 2020). As will be discussed later in section 4, the high thermal gradients associated with the process provide unfavourable conditions for a columnar-to-equiaxed transition (Hunt, 1984). Since the process parameters have a little influence on the size and fraction, a hypothesis might be that they condensate from the plasma created with the keyhole during the process.

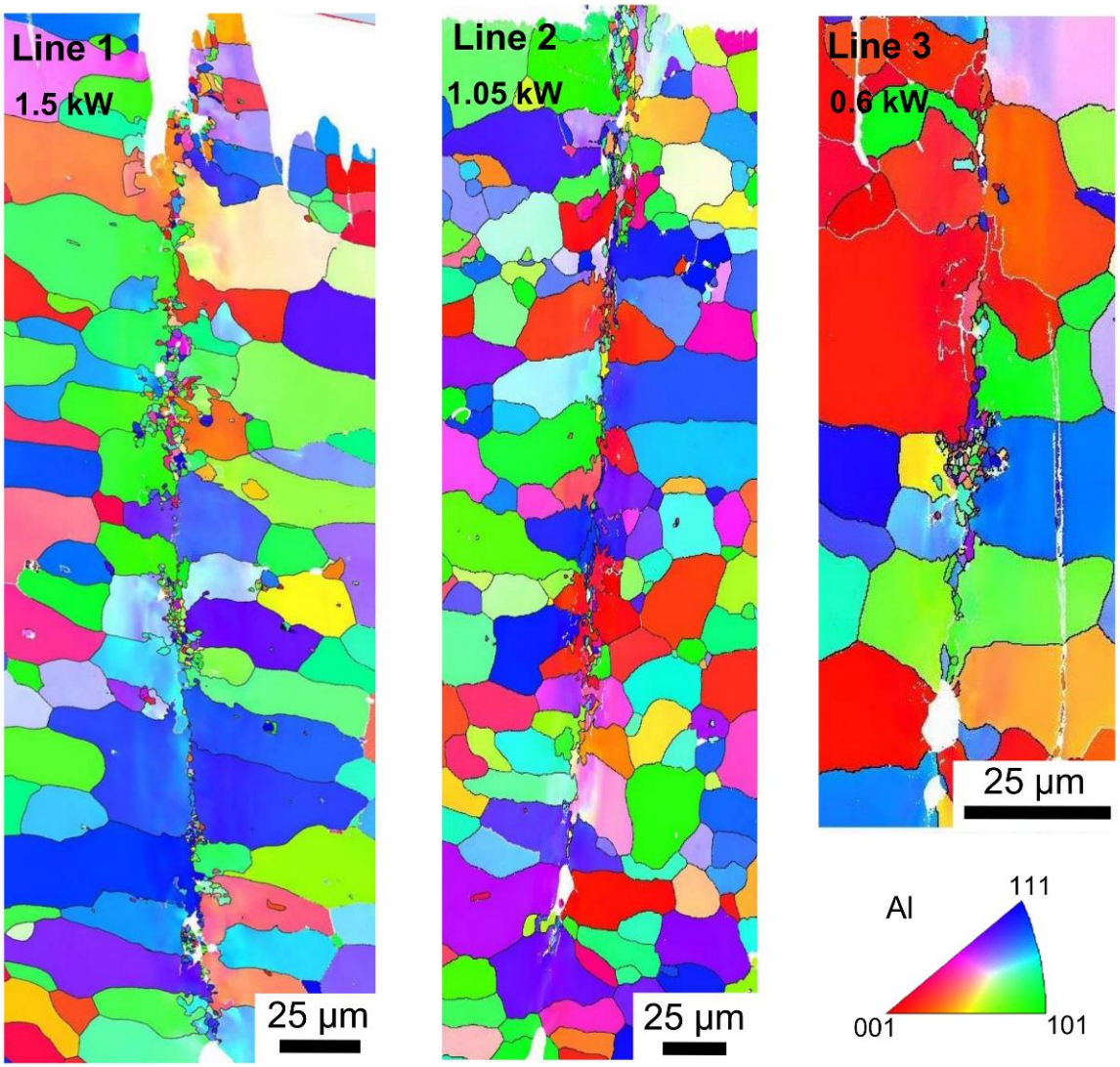

Fig. 6. EBSD analysis of the microstructure of fusion lines obtained at varied peak power and pulse duration of 200 ns.

Table 3
Fusion zone grains parameters measured by EBSD analysis.

Fusion line number	P_{AP}, kW	Grain size, μm	Surface fraction of grains*, %
1	1.5	1,25 ± 0,81	9.42
2	1.05	1,60± 0.99	9.93
3	0.6	1,23 ± 0,81	7.42

* the surface fraction was calculated for each line as the ratio of the area of all detected grains to the area of the welded zone, calculated according to the data in Table 2

4. Discussion

Several questions remain unaddressed so far, such as the lack of a dendritic microstructure, the supersaturated Al solid solution or the absence of solidification cracking. Elements of answers can come from an in-depth analysis of the phenomena.

The lower limit of the thermal gradient and cooling rate associated with the process can be estimated through the geometrical analysis of the fusion lines. Since the keyhole mode was reached, the temperature at the centre of the liquid capillary is at minimum, the vaporization temperature of the alloy, T_v, taken as 2327°C (Wang et al., 2019). The temperature at the base material/weld pool interface is assumed to be the alloy solidus temperature, T_s, calculated to be 601°C by thermodynamic calculations. From the weld pool geometry, the thermal gradient, G_T, can be estimated using Eq. 1:

$$G_T = \frac{T_v - T_S}{W/2} \quad (1)$$

Where W is the width of the weld pool. The cooling rate $\dot{T}$ can be estimated as the product of G_T and the laser scanning velocity V, $\dot{T} = G_T.V$. To give order of magnitude, for a 30 µm width weld pool, the thermal gradient is of the order of G_T=1.15 10^8 K/m and the associated cooling rate is $\dot{T}$=4.6 10^6 K/s. While the cooling rate is similar to those observe in powder-based laser additive manufacturing techniques (Bertoli et al., 2017), the thermal gradient associated with the nano-second pulsed laser processing in very high, reminding that the order of magnitude given here represent a lower limit. One can now wonder how such high thermal gradient would affect the microstructure formation.

Microstructure of fcc-Al phase has been modeled using the interface response functions developed by Kurz (2001). In this approach, the growth behavior of plane front and cells/dendrites is calculated; it can determine the phase and the growth form which develops at the highest interface temperature for a given growth velocity and temperature gradient.

Neglecting the attachment kinetics for fcc-Al growth in the present treatment because the interface velocities are relatively low and of the rough interface nature of aluminum at the atomic scale, the planar front interface temperature T_p is given by Eq.2:

$$T_p = T_m + \sum_i C_0^i \frac{m_{L,i}^v}{k_i^v} \quad (2)$$

Where T_m is the pure aluminum melting temperature, i denotes the alloying elements (i=Mg, Si, Cu, Fe), C_0^i is the wt.% concentration of i and $m_{L,i}^v$ and k_i^v are the kinetic liquidus slopes and partition coefficients, as defined first by Boettinger et al. (1984) and later by Aziz (1996). For the cellular/dendritic growth, the interface temperature is given by Eq.3:

$$T_d = T_L - \left[\Delta T_C + \sum_i C_0^i (m_{L,i} - m_{L,i}^v) + \frac{2\Gamma}{R} + \frac{G_T . D_L}{V}\right] \quad (3)$$

Where $T_L = T_m + \sum_i C_0^i m_{L,i}^v$ is the liquidus temperature of the alloy, ΔT_C is the constitutional undercooling at the dendrite tip, $\sum_i C_0^i \left(m_{L,i} - m_{L,i}^v\right)$ is the modification of the equilibrium phase diagram by solute trapping, $2\Gamma/R$ is the curvature undercooling (with Γ the Gibbs-Thomson constant and R the dendrite tip radius) and $G_T D_L/V$ is the cell tip undercooling (with D_L a liquid diffusion coefficient taken as 5.10^{-9} m^2/s and V the interface velocity). The constitutional undercooling has been determined using the KGT model for multicomponent alloys developed by Kurz et al. (1986). Equilibrium liquidus slopes and partition coefficients were determined using the Thermo-Calc software and the TTAL5 database.

The results are presented in Fig. 7 for velocities ranging from 1 µm/s to 10 m/s and for different temperature gradient: (i) 10^4 K/s which is typical of conventional casting processes, (ii) 10^6 K/s which is relevant for LBPF AM processes, (iii) 1.85 10^8 K/m which corresponds to the estimate thermal gradient for line 6, and (iv) 2.2 10^8 K/s which correspond to the critical value for which no dendritic pattern can form in the present processing range. In this Fig., the velocities encountered in nano-second pulsed laser process we used is indicated by

the grayed-out rectangle, and range from ≈ 6 mm/s close to base material / melt pool interface to 40 mm/s which is the laser beam velocity. The arrows at the bottom of the Fig. indicate the onset of the planar to cell/dendrite transition at low velocity with the same color code than for the considered thermal gradient. From this Fig., it can be seen that for the lowest gradient, cellular/dendritic microstructure is the most stable morphology from V=1µm/s up to a velocity of 250 mm/s. For G_T=10^6 K/s, the velocity range for which cells/dendrite can be observed is already narrower, from 0.1 to 250 mm/s. For the thermal gradient estimated from the present microstructure analysis, i.e. 1.85 10^8 K/s, the velocity range, indicated by the red rectangle in the Fig., is between 25 and 100 mm/s. When superimposing this range with the velocities achievable with the process, only a small window ranging between 25 and 40 mm/s would allow dendritic growth. For the same gradient, another remark is that the temperature difference between the dendrite tip (upper part of the red curve) and the solidus temperature, i.e. the solidification interval upon the mushy zone, is at maximum ΔT = 6°C. compared to the thermal gradient, this corresponds to a length of $\Delta T/G_T$ = 32 nm. It is thus impossible, with such high gradient to form a dendritic microstructure with our process. Also, as already mentioned earlier, the thermal gradients that were evaluated from the microstructure are probably under-estimated and correspond to a lower possible limit, since the temperature in the keyhole is probably higher than the vaporization temperature of the alloy. In Fig. 7, the calculation for the highest value of the gradient correspond to the value for which no dendritic pattern is expected in the processing range. It corresponds to a value G_T=2.2 10^8 K/s which is close to the value we estimated. The reader should also note that above this value, the planar front is the only interface morphology that remains stable.

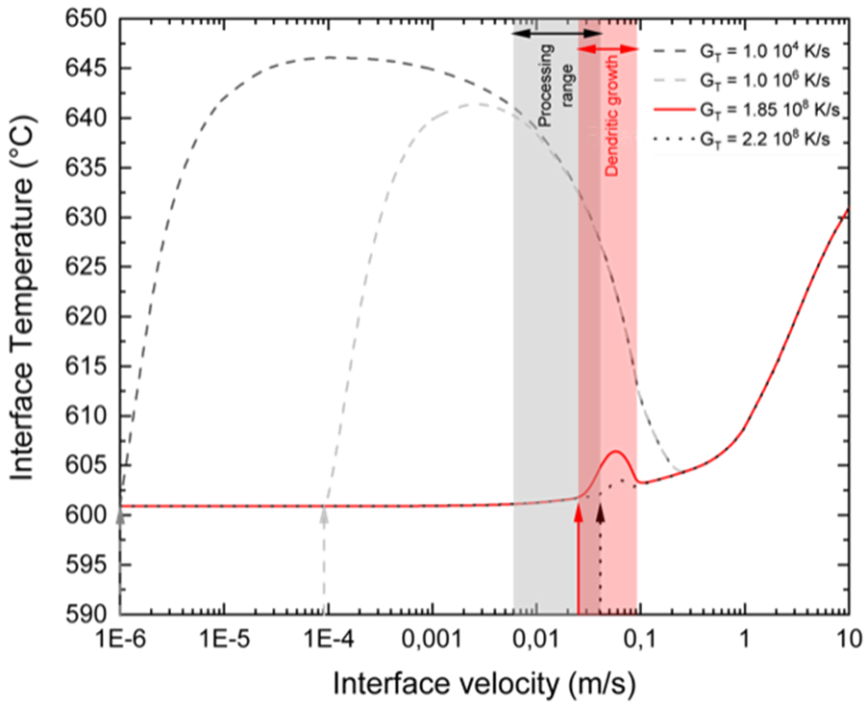

Fig.7. Modeling of interface temperatures for planar and cellular microstructures during nano-second pulsed laser processing of AA6061

Such analysis shows that with the thermal gradients encountered with this process, it is very unlikely to form a dendritic structure. This explains the absence of dendritic microstructure observed experimentally, but also the lack of microsegregations in the weld pool. Least but not last, it also explains why the alloy was not prone to solidification cracking. Indeed, solidification cracking is usually observed when the thermal stresses induce strain in the mushy zone for solid fractions between 0.8 and 0.96 (these values might slightly change depending on the alloy), where liquid feeding is not sufficient. This leads to a local pressure drop that lead to cracking under stress (Rappaz et al., 1999). With the current processing conditions, there is no mushy zone and the model only predicts a planar interface, which is coherent with our observations. Such conditions thus suppress the well-known cracking susceptibility of theses alloys, opening new prospects for joining AA6XXX without filler material.

5. Conclusions

In this work, AA6061 was processed with a nano-second pulsed laser welding in keyhole mode. In-depth microstructure characterisation associated with solidification microstructure modelling lead to the following conclusions. The only defect found in the welds were porosity, which fraction can be decreased by decreasing the average peak power. For all the processing conditions tested, the microstructure did not show any dendritic microstructure and any segregation patterns. The grain structure was composed of grains that have grown by epitaxy from the base material and a fine equiaxed region at the centreline. The geometrical characterisation of the weld pools leads to the estimate of very high thermal gradients, typically greater than 10^8 K/s. Under such condition, microstructure modeling has confirmed that dendritic growth is very unlikely, and predict a planar front solidification. This solidification mode suppresses the solidification cracking since there is no mushy zone anymore, making nano-second pulsed laser welding a promising route for so far non-weldable alloys.

Acknowledgements

The authors thank F. Machi and A. Fritsch at IREPA LASER for performing laser processing of the samples. D.Z. is gratefull to the Région Grand Est for funding her fellowship under grant No. N°19P11049.

References

Abioye, T. E., Zuhailawati, H., Aizad, S., Anasyida, A.S., 2019. Geometrical, microstructural and mechanical characterization of pulse laser welded thin sheet 5052-H32 aluminum alloy for aerospace applications. Trans. Nonferrous Met. Soc. China 29, 667−679.

Ascari, A., Fortunato, A., Guerrini, G., Liverani, E., Lutey, A., 2017. Long Pulse Laser Micro Welding of Commercially Pure Titanium Thin Sheets. Procedia Eng. 184, 274 – 283.

Assuncao, E., Williams, S., 2013. Comparison of continuous wave and pulsed wave laser welding effects. Optics and Lasers in Engineering 51, 674–680.

Aziz, M. J.,1996. Interface attachment kinetics in alloy solidification. Metall. Mater. Trans. A 27, 671-686.
Bergmann, J. P., Bielenin, M., Stambke, M., Feustel, T., Witzendorff, P.V., Hermsdorf J., 2013. Effects of diode laser superposition on pulsed laser welding of aluminum. Physics Procedia 41, 180 – 189.
Bertoli, U.S., Guss, G., Wu, S., Matthews, M.J., Schoenung, J.M., 2017. In-situ characterization of laser-powder interaction and cooling rates through high-speed imaging of powder bed fusion additive manufacturing. Mater. Des. 135, 385-396.
Boettinger, W.J., Coriell, S.R., Sekerka, R.F., 1984. Mechanisms of microsegregation-free solidification. Mater. Sci. Eng.: A 65, 27-36.
Çam, G., İpekoğlu, G., 2017. Recent developments in joining of aluminum alloys. Int. J. Adv. Manuf. Technol. 91, 1851–1866.
Chua, S.F., Chen, H-C., Bi, G., 2019. Influence of pulse energy density in micro laser weld of crack sensitive Al alloy sheets. J. Manuf. Process. 38, 1–8.
Cieslak, M.J., Fuerschbach, P.W., 1988. On the weldability, composition and hardness of pulsed and continuous Nd-YAG laser welds in aluminum-alloys 6061, 5456 and 5086. Metall. Trans. B 19, 319–29.
El-Batahgy, A., Kutsuna, M., 2009. Laser Beam Welding of AA5052, AA5083, and AA6061 Aluminum Alloys. Advances in Mater. Sci. Eng. 7, 974182.
Fabbro, R., Chouf K., 2000. Dynamical description of the keyhole in deep penetration laser welding. J. Laser Appl. 12, 142-148.
Fahimpour, V., Sadrnezhaad, S.K., Karimzadeh, F., 2012. Corrosion behaviour of aluminum 6061 alloy joined by friction stir welding and gas tungsten arc welding methods. Mater. Des. 39, 329–333.
Gabzdyl, J., Rosowski, A., 2017. Welding thin section dissimilar metals with ns pulsed fiber lasers. Lasers in Manufacturing Conference.
Haboudou A., Peyre, P., Vannes, A.B., Peix, G., 2003. Reduction of porosity content generated during Nd:YAG laser welding of A356 and AA5083 aluminum alloys. Mater. Sci. Eng.: A 363, 40–52.
Hagenlocher, C., Weller, D., Weber, R., Graf, T., 2019. Reduction of the hot cracking susceptibility of laser beam welds in AlMgSi alloys by increasing the number of grain boundaries. Science and technology of welding and joining 24, 313–319.
Hosseinifar, M., Malakhov, D.V., 2011. The Sequence of Intermetallics Formation during the Solidification of an Al-Mg-Si Alloy Containing La. Metall. Mater. Trans. A 42, 825–33.
Hunt, J.D., 1984. Steady state columnar and equiaxed growth of dendrites and eutectic. Mater. Sci. Eng. 65, 75-83.
Kelkar, G., 2008. Pulsed laser welding. Mater. Sci., 44225117.
Kim, J., Ki, H., 2014. Scaling law for penetration depth in laser welding. J. Mater. Process. Technol. 214, 2908–2914.
Kuo, T.Y., Lin, H.C., 2006. Effects of pulse level of Nd-YAG laser on tensile properties and formability of laser weldments in automotive aluminum alloys. Mater. Sci. Eng.: A 416, 281–289.
Kurz, W., 2001. Solidification Microstructure-Processing Maps: Theory and Application. Adv. Eng. Mat. 3, 443-452.
Kurz, W., Giovanola, B., Trivedi, R., 1986. Theory of microstructural development during rapid solidification. Acta Metall. 34, 823–830.
Löveborn D., Larsson J. K., Persson K. A., 2017. Weldability of Aluminum Alloys for Automotive Applications. Physics Procedia 89, 89-99.
Mainman, T.H., 1960. Stimulated Optical Radiation in Ruby. Nature 187, 493-494.

Rappaz, M., Drezet, J. M., Gremaud, M., 1999. A new hot-tearing criterion. Metall. Mater. Trans. A 30, 449-455.

Rappaz, M., Jarry, Ph., Kurtuldu, G., Zollinger, J., 2020. Solidification of Metallic Alloys: Does the Structure of the Liquid Matter? Metall. Trans. A 51, 2651–2664.

Schmidt, M., Zaeh, M., Li L., Duflou, J., Overmeyer, L., Vollertsen, F., 2018. Advances in macro-scale laser processing. CIRP Annals - Manufacturing Technology 67, 719–742.

Tang, Z., Vollertsen, F., 2014. Influence of grain refinement on hot cracking in laser welding of aluminum. Weld World 58, 355–366.

Wang, L., Gao, M., Zeng, X., 2019. Experiment and prediction of weld morphology for laser oscillating welding of AA6061 aluminum alloy. Sci. Technol. Weld. Join. 24, 334-341.

Wang, L., Gao, M., Zhang, C. & Zeng, X., 2016. Effect of beam oscillating pattern on weld characterization of laser welding of AA6061-T6 aluminum alloy. Materials & Design 108, 707–717.

Yusof, M.F.M., Ishak M., Ghazali, M.F., 2021.Weld depth estimation during pulse mode laser welding process by the analysis of the acquired sound using feature extraction analysis and artificial neural network. J. Manuf. Process. 63, 163–178.